Ordinary-differential-equation-based nonequilibrium wall modeling for large-eddy simulation

Ryo Kamogawa, Yoshiharu Tamaki, and Soshi Kawai*
Department of Aerospace Engineering, Tohoku University, Sendai, Miyagi 980-8579, Japan

(Received 2 November 2022; accepted 15 May 2023; published 9 June 2023)

This paper proposes an ordinary-differential-equation (ODE)-based nonequilibrium boundary layer (NEQBL) wall modeling in large-eddy simulation (LES) for accurate prediction of nonequilibrium separated turbulent boundary layers at a high Reynolds number. The proposed ODE-based wall model does not require computational grids with full connectivity. The key to the modeling is to incorporate the nonequilibrium effects into the pressure-gradient term, convective term, and turbulent eddy viscosity consistently. The model is inaccurate if any of these terms are modeled inconsistently from the others, and it is found important to include the nonequilibrium effects into the turbulent eddy viscosity, which has not been discussed in prior studies. The proposed modeling of the three nonequilibrium terms is first analyzed by *a priori* tests using the wall-resolved LES (WRLES) database of pressure-induced separated and reattached turbulent boundary layer at Reynolds number $\mathrm{Re}_\theta \approx 2.0 \times 10^3$. Then, the wall-modeled LES using the proposed ODE-based NEQBL wall model is conducted under the same condition as the WRLES database. The proposed ODE-based NEQBL model yields accurate predictions of the resolved turbulence statistics for both equilibrium-attached and nonequilibrium-separated flows.

DOI: 10.1103/PhysRevFluids.8.064605

I. INTRODUCTION

Accurate prediction of separated turbulent boundary layers is one of the crucial factors in the design of many industrial applications, such as aircraft, rockets, turbines, etc. Large-eddy simulation (LES) is a promising approach to predicting the separated turbulent boundary layers since energetic and dynamically important eddies are directly resolved. However, the computational cost of the wall-resolved LES (WRLES) of wall-bounded turbulent flows at a high Reynolds number becomes highly prohibitive [1–3], which leads to the wall-modeled LES (WMLES; cf. the review articles [4–6]) for predicting the high Reynolds number wall-bounded flows. In the WMLES, the spatially filtered LES equations are solved on the computational grid that resolves outer-layer turbulence, while the effects of the unresolved near-wall turbulence in the inner layer (i.e., the innermost approximately 10% of the boundary layer, $y \lesssim 0.1\delta$) are modeled to alleviate the near-wall grid resolution requirement in viscous units. In the wall-stress modeling approach (e.g., Refs. [7–14]), an inner-layer wall model that is solved between the wall and wall-model top boundary (i.e., the matching location $y = h_{\mathrm{wm}}$) estimates the wall-shear stress τ_w (and wall heat flux q_w for compressible flows) and imposes τ_w (and q_w) as a flux boundary condition for the LES. Since the LES resolves the outer-layer turbulence (say, in the region $y \gtrsim 0.1\delta$) directly, the key to the accurate prediction of the WMLES is the modeling of the inner-layer turbulence.

*Corresponding author: kawai@tohoku.ac.jp

One of the simplest and most prevalent wall-stress models is the equilibrium boundary layer (EQBL) model [7,8,10,12]. The EQBL model solves the equilibrium boundary layer equation:

$$\frac{d}{dy}\left[(\overline{\mu}+\overline{\mu}_t)\frac{d\overline{u}}{dy}\right]=0, \tag{1}$$

where u is the wall-parallel velocity, μ is the shear viscosity, and μ_t is the turbulent eddy viscosity. Equation (1) is derived from the Favre-averaged momentum equation by imposing the equilibrium assumptions. The Favre-averaged momentum equation is

$$\overline{\rho}\frac{\partial\widetilde{u}_i}{\partial t}+\overline{\rho}\widetilde{u}_j\frac{\partial\widetilde{u}_i}{\partial x_j}+\frac{\partial\overline{p}}{\partial x_i}=\frac{\partial\overline{\tau}_{ij}}{\partial x_j}-\frac{\partial}{\partial x_j}(\overline{\rho}\widetilde{u_i''u_j''}), \tag{2}$$

where ρ is the density, u_i is the velocity components, p is the static pressure, τ_{ij} is the viscous stress tensor, $\overline{f}$ and $\widetilde{f}$ denote the Reynolds and Favre averaging quantities, $f=\overline{f}+f'$ and $f=\widetilde{f}+f''$. The EQBL model employs the equilibrium assumptions, where the time-derivative, convective, pressure-gradient, and wall-parallel viscous-diffusion terms in Eq. (2) are neglected. Also, in the EQBL model, the Reynolds shear stress is modeled by the Boussinesq eddy-viscosity approximation $-\overline{\rho}\widetilde{u''v''}\approx\overline{\mu}_t(d\overline{u}/dy)$. Consequently, the EQBL model solves the wall-normal ordinary differential equation (ODE) between the wall and matching location $y=h_{\mathrm{wm}}$ and thus allows the model to be applied without the computational grids with full connectivity in all directions.

The WMLES with the EQBL model has been widely used to simulate attached equilibrium boundary layer flows [12,15] and also separated nonequilibrium boundary layer flows [16–23] at high Reynolds numbers. In most cases, the EQBL wall model reasonably predicts the low-order turbulent statistics (e.g., the mean velocity, Reynolds stresses, etc.) even for the separated nonequilibrium flows where the equilibrium assumptions used in the EQBL model are no longer valid. However, some prior studies [11,19,24,25] reported that the neglected nonequilibrium terms (hereafter, called the nonequilibrium effects) become important in predicting the nonequilibrium boundary layers such as separated turbulent boundary layers. Wang and Moin [11] showed that the model including the nonequilibrium effects improves the skin-friction prediction near the airfoil trailing edge where the pressure gradient is nonnegligible. Similarly, Tamaki *et al.* [19] showed the nonnegligible contributions of the nonequilibrium effects near the airfoil leading-edge where the pressure gradients are present. Also, Park [25] indicates that the equilibrium assumptions are not valid in a separation bubble and downstream of the reattachment, and the wall model including the nonequilibrium effects improves the prediction accuracy.

To incorporate the nonequilibrium effects into the wall model, a straightforward approach is to solve some form of the RANS (Reynolds averaged Navier-Stokes)-type partial differential equations (PDEs) that include the nonequilibrium effects without the use of the equilibrium assumptions [9,10,13,14]. Because of the PDE-based governing equations used in the nonequilibrium boundary layer (NEQBL) model, the NEQBL model requires the wall-layer mesh between the wall and matching location $y=h_{\mathrm{wm}}$ with full connectivity in all directions, which often increases the difficulty of using the NEQBL model for complex geometries. To remove the full connectivity required for solving the PDE-based NEQBL model, the developments of the ODE-based [11,24,26,27] or machine-learning-based [28] NEQBL models that do not require the wall-layer mesh have been attempted. In the ODE-based models, to reduce the PDE to an ODE, the nonequilibrium effects are modeled by using the outer-layer LES solutions at the wall-model top boundary (i.e., at the matching location $y=h_{\mathrm{wm}}$). Hoffmann and Benocci [26], Wang and Moin [11], and Catalano *et al.* [27] modeled the pressure-gradient term without modeling the convective term. However, Hickel *et al.* [24] proposed an ODE-based NEQBL model that accounts for both the pressure-gradient and convective terms and argued that the consistent modeling between the convective and pressure-gradient terms is the key to accurate modeling of the nonequilibrium effects. Also, there is a potential issue with the turbulent eddy viscosity modeling used in the wall model [19], which has not been discussed in prior studies. In the existing PDE-based [9,10,13,14] and ODE-based [11,24,26,27] NEQBL models, the

turbulent eddy viscosity used in the wall model is calculated using the mixing-length model derived from the equilibrium assumptions. A recent study by Tamaki *et al.* [19] suggested that the turbulent eddy viscosity modeling also needs to be modified for the NEQBL model to maintain consistency with the nonequilibrium effects. Therefore, there is a potential inconsistency between the modeling of the nonequilibrium terms (i.e., the pressure-gradient and convective terms) and the turbulent eddy viscosity when using the mixing-length model.

In this study, we propose an ODE-based NEQBL wall model for the LES at a high Reynolds number by consistently modeling the nonequilibrium effects, i.e., the pressure-gradient and convective terms, and the turbulent eddy viscosity. The proposed model only requires the input from the outer-layer LES at the matching location $y = h_{\mathrm{wm}}$ and does not require grid connectivity, which is typically needed for the existing PDE-based NEQBL models [9,10,13,14], and thus does not require the wall-layer mesh to compute the NEQBL wall model. We first analytically derive the consistent modeling for the nonequilibrium effects term-by-term and then validate the derived modelings through *a priori* tests and numerical experiments (in which the proposed ODE-based NEQBL wall model is implemented to the solver) by comparing with the WRLES database of a nonequilibrium pressure-induced separated and reattached turbulent boundary layer. Since a high-fidelity turbulence database plays an essential role in the modeling and validation processes, the WRLES of the separated and reattached turbulent boundary layer at moderately high Reynolds number $\mathrm{Re}_\theta \approx 2.0 \times 10^3$ (and freestream Mach number $M_\infty = 0.2$) with 1.6 billion grid points is conducted, and the obtained high-fidelity WRLES database is analyzed. Using the direct comparisons between the WRLES database and modeling of the nonequilibrium effects, the detailed analysis of the nonequilibrium terms in the inner layer can be addressed for developing the physics-based modeling.

This paper is organized as follows. In Sec. II, we first describe the reference WRLES database of pressure-induced separated and reattached turbulent boundary layer on a flat plate (the WRLES database is available on our website [29]). Then, the ODE-based modeling of the pressure-gradient and convective terms, and the turbulent eddy viscosity are analytically derived, and each model is validated based on the WRLES database. At the end of Sec. II, the framework of the proposed ODE-based NEQBL wall model is summarized. In Sec. III, the proposed ODE-based NEQBL model is validated through *a priori* tests using the WRLES database. Then, the prediction capability of the WMLES with the proposed ODE-based NEQBL wall model for the attached and separated turbulent boundary layers is discussed in Sec. IV. The concluding remarks are provided in Sec. V.

II. ODE MODELING OF NONEQUILIBRIUM EFFECTS

The proposed ODE-based NEQBL wall model consists of the modelings of the pressure-gradient term, convective term, and turbulent eddy viscosity. The governing equation for the ODE-based NEQBL model is derived from the streamwise momentum equation (Eq. (2)). First, the thin-boundary-layer approximation is applied to Eq. (2), i.e., ignoring $\partial/\partial x$ and $\partial/\partial z$ terms in the right-hand-side viscous and Reynolds stress terms,

$$\overline{\mathrm{Conv.}} + \overline{\mathrm{Pres.}} = \frac{d}{dy}\left(\overline{\mu}\frac{d\overline{u}}{dy}\right) + \frac{d}{dy}(-\overline{\rho}\widetilde{u''v''}), \tag{3}$$

where $\overline{\mathrm{Conv.}}$ is the convective term [$\overline{\mathrm{Conv.}} \equiv \overline{\rho}\tilde{u}(d\tilde{u}/dx) + \overline{\rho}\tilde{v}(d\tilde{u}/dy)$], $\overline{\mathrm{Pres.}}$ is the streamwise pressure-gradient term ($\overline{\mathrm{Pres.}} \equiv d\overline{p}/dx$), u and v are the streamwise and wall-normal velocity, and x and y are the streamwise and wall-normal direction. Note that neglecting the streamwise diffusion term assumes a mild streamwise change of the flow. We have confirmed that the streamwise diffusion term is negligible in the present low-speed gradually separated flow. Then, applying the Boussinesq approximation to the Reynolds shear stress yields

$$\frac{d}{dy}\left[(\overline{\mu} + \overline{\mu}_t)\frac{d\overline{u}}{dy}\right] = \overline{\mathrm{Conv.}} + \overline{\mathrm{Pres.}} \tag{4}$$

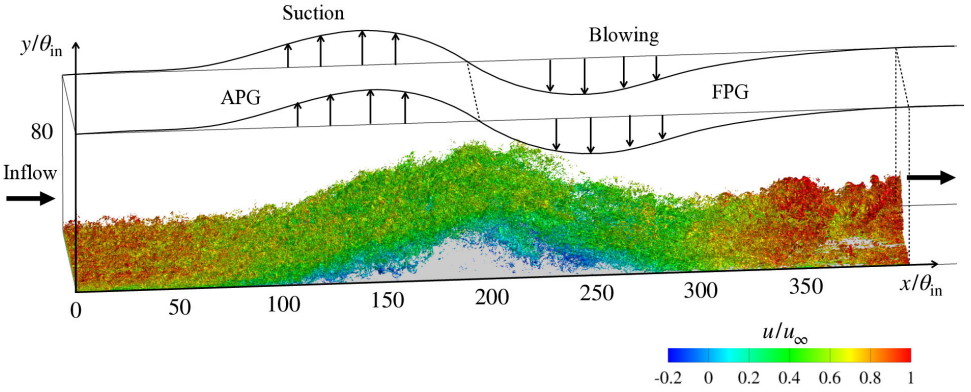

FIG. 1. Schematic of separated and reattached turbulent boundary layer on a flat-plate with adverse and favorable pressure gradients (APG and FPG). Isosurfaces of instantaneous $Q \equiv -(1/2)(\partial u_i/\partial x_j)(\partial u_j/\partial x_i) = 0.03u_\infty^2/\theta_{in}^2$ colored by streamwise velocity u.

In the ODE-based NEQBL model, the nonequilibrium effects ($\overline{\text{Conv.}}$, $\overline{\text{Pres.}}$, and $\overline{\mu_t}$) in Eq. (4) are consistently modeled based on the theoretical analyses and the WRLES database. In this section, the high-fidelity WRLES database is described in Sec. II A. Then, in Sec. II B, the modeling of the nonequilibrium effects, i.e., the pressure-gradient term, convective term, turbulent eddy viscosity, and *a priori* analyses of the proposed modelings are discussed.

A. Wall-resolved LES database [29]

To analyze and validate the proposed modeling of the nonequilibrium effects in detail, the WRLES of a pressure-induced separated and reattached turbulent boundary layer on a flat plate at the Reynolds number based on the inlet momentum thickness $\text{Re}_{\theta_{in}} \approx 2000$ and inlet freestream Mach number $M_\infty = 0.2$ is conducted. The simulation settings are following Na and Moin [30] and Abe [31], but the Reynolds number is increased so that the scales of the inner and outer layers more clearly separate. Following the previous studies [30–32], the streamwise pressure gradient is generated by imposing the wall-normal velocity at the upper boundary as

$$v_{top} = v_{max} \times \sqrt{2} \times \left(\frac{x_c - x}{\sigma}\right) \exp\left[\psi - \left(\frac{x_c - x}{\sigma}\right)^2\right], \tag{5}$$

where $v_{max}/u_\infty = 0.3325$, $x_c/\theta_{in} \approx 10^5/2^9$, $\sigma/\theta_{in} \approx 80\sqrt{2}(5^2/2^5)$, $\psi = 0.95$, and θ_{in} is the momentum thickness at the inlet of the computational domain (test section) shown in Fig. 1. Similar to the prior studies [33,34], the inflow turbulence for the test section is extracted from the concurrent WRLES of the nominally zero-pressure-gradient fully developed flat-plate turbulent boundary layer computed in the separated domain (driver section, not shown in Fig. 1). The rescaling-reintroduction method [35] is used to generate realistic inflow turbulence in the driver section. The size of test section in Fig. 1 is $L_x \approx 400\theta_{in}$, $L_y \approx 80\theta_{in}$, and $L_z \approx 80\theta_{in}$ in streamwise (x), wall-normal (y), and spanwise (z) directions, and the driver section is $L_x \approx 172\theta_{in}$, $L_y \approx 80\theta_{in}$, and $L_z \approx 80\theta_{in}$, where the subscript (in) denotes the inlet quantity of the test section. Note that in the test section, an additional buffer region with the length of $800\theta_{in}$ in the streamwise direction is placed at the outlet boundary to remove turbulent fluctuations and any reflections from the boundary (i.e., the actual computational domain size of the test section is $L_x \approx 1200\theta_{in}$, $L_y \approx 80\theta_{in}$, and $L_z \approx 80\theta_{in}$). The total number of grid points for the test section is approximately 1.6 billion. Here, the wall-tangential grid spacings are $\Delta x^+ \approx 12.6$ and $\Delta z^+ \approx 6.3$, while the wall-normal grid spacing Δy^+ is approximately 0.8 at the wall and does not exceed 13 in the region $y/\theta_{in} \lesssim 40$. Note that the superscript $+$ denotes a quantity in wall units. The same grid spacing is also used in the driver section. The present grid resolution is sufficient for the WRLES to resolve the near-wall turbulent structures with the employed sixth-order

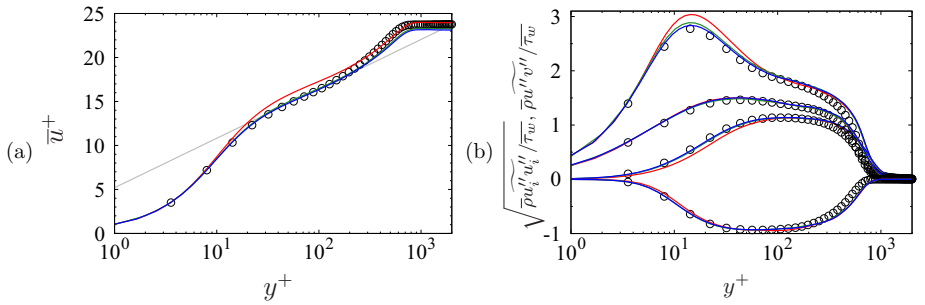

FIG. 2. Inflow turbulence statistics obtained by the WRLES of pressure-induced separated and reattached turbulent boundary layer on a flat plate at $\mathrm{Re}_{\theta_{\mathrm{in}}} \approx 2000$ and $M_\infty = 0.2$. (a) Mean streamwise velocity, (b) Reynolds stresses: upper, $\sqrt{\widetilde{\rho u'' u''}/\overline{\tau}_w}$; upper-middle, $\sqrt{\widetilde{\rho w'' w''}/\overline{\tau}_w}$; lower-middle, $\sqrt{\widetilde{\rho v'' v''}/\overline{\tau}_w}$; lower, $\widetilde{\rho u'' v''}/\overline{\tau}_w$. Blue lines, present WRLES with $\Delta x^+ \approx 12.6$, $\Delta y^+ \lesssim 12.6$, and $\Delta z^+ \approx 6.3$; green lines, WRLES with $\Delta x^+ \approx 15$, $\Delta y^+ \lesssim 15$, and $\Delta z^+ \approx 7.5$; red lines, WRLES with $\Delta x^+ \approx 26$, $\Delta y^+ \lesssim 26$, and $\Delta z^+ \approx 13$; circles, incompressible DNS at $\mathrm{Re}_\theta = 2000$ [37]; gray line in (a), $\overline{u}^+ = 1/0.41 \log(y^+) + 5.2$.

compact difference scheme [36]. Figure 2 shows that the grid-converged turbulence statistics of the mean streamwise velocity and Reynolds stresses are achieved by the employed grid (i.e., the finest grid in Fig. 2), and the turbulent statistics at the inlet show a good agreement with the direct numerical simulation (DNS) of an incompressible turbulent boundary layer at $\mathrm{Re}_\theta = 2000$ [37].

The spatial derivatives are evaluated by the sixth-order compact difference scheme [38] coupled with an eighth-order low-pass filter [38,39] where the filter parameter α_f is fixed at 0.495. Our prior studies [33,36] indicate the appropriateness of applying $\alpha_f = 0.495$ for high-fidelity turbulent flow simulations. The explicit third-order total variation diminishing Runge-Kutta scheme [40] is used for time integration. The subgrid-scale (SGS) turbulent eddy viscosity is calculated by the selective mixed-scale model [41]. After the flow reaches a quasi-steady state, the turbulence statistics are computed by averaging in time for a time interval of $1600\theta_{\mathrm{in}}/u_\infty$ as well as in the homogeneous spanwise direction to ensure convergence of flow statistics.

Figure 3 compares the skin friction and mean streamwise velocity obtained by the present WRLES with the available DNS database at lower Reynolds number $\mathrm{Re}_{\theta_{\mathrm{in}}} = 900$ by Abe [31]. The WRLES shows the separated and reattached flow similar to the DNS, although the upstream and downstream skin friction shows some discrepancies because of the different Reynolds numbers employed by the present WRLES and the DNS (although not shown here, we also conduct the WRLES at $\mathrm{Re}_{\theta_{\mathrm{in}}} = 900$ and the results well agree with the results of the incompressible DNS by Abe [31]). By using the WRLES database [29], the nonequilibrium terms in the inner layer are analyzed in details and the modelings of the nonequilibrium effects are validated through the direct comparisons.

B. Modeling of nonequilibrium effects and *a priori* analyses

1. Pressure-gradient term

To model the pressure-gradient term ($\overline{\mathrm{Pres.}} = d\overline{p}/dx$) in Eq. (4) in the inner layer, the typical boundary layer theory, constant pressure in the wall-normal direction throughout the wall-modeled layer is employed. Therefore, using the pressure in the outer-layer LES solutions at the matching location h_{wm}, the pressure-gradient term is modeled as

$$\overline{\mathrm{Pres.}}_{\mathrm{model}} = \left.\frac{d\overline{p}}{dx}\right|_{h_{\mathrm{wm}}}. \tag{6}$$

This modeling is the same as the modeling proposed by Wang and Moin [11] and Hickel *et al.* [24]. We note that the assumption of the constant pressure in the wall-normal direction is widely employed by the wall modeling and is also assumed in the derivation of the EQBL model [12].

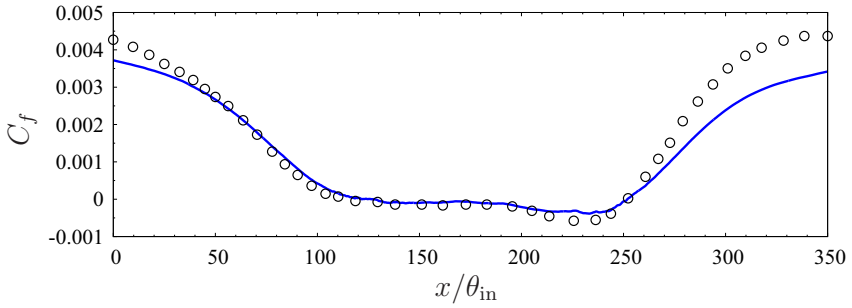

(a) Skin friction coefficient (blue line, present WRLES; circles, incompressible DNS[31])

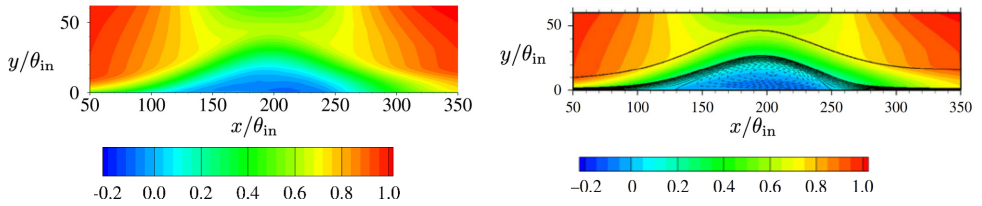

(b) Streamwise velocity $\tilde{u}/u_\infty$ (left, present WRLES; right, incompressible DNS[31])

FIG. 3. Comparisons between the present WRLES database [29] at $\mathrm{Re}_{\theta_{\rm in}} = 2000$ and the available incompressible DNS [31] at lower Reynolds number $\mathrm{Re}_{\theta_{\rm in}} = 900$ for pressure-gradient-induced separated and reattached turbulent boundary layer.

The modeling of Eq. (6) is validated through *a priori* tests using the WRLES database [29]. Figure 4 compares the proposed pressure-gradient model $\overline{\mathrm{Pres.}}_{\rm model}$ with the WRLES database of $d\overline{p}/dx$ below the matching location $h_{\rm wm}$ (where the matching location is set to $h_{\rm wm} \approx 0.85\theta_{\rm in}$ that is approximately 10% of the boundary layer thickness) at the streamwise locations $x/\theta_{\rm in} = 0$, 50, 100, 150, 200, 250, 300, 350. The WRLES database indicates the almost constant distributions of the pressure-gradient term in the wall-normal direction and almost zero pressure gradient at the inlet and separated region $x/\theta_{\rm in} = 0$, 150, 200, 250, adverse pressure gradient at the upstream region $x/\theta_{\rm in} = 50$, 100, and favorable pressure gradient at the downstream reattached region $x/\theta_{\rm in} = 300$, 350. The proposed model well predicts these streamwise variations of the pressure-gradient term.

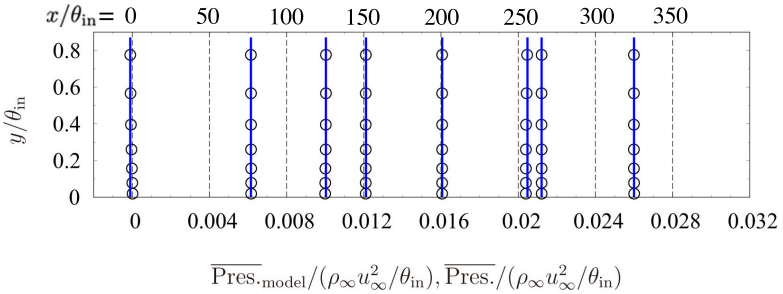

FIG. 4. *A priori* test of the proposed modeling of the pressure-gradient term at $x/\theta_{\rm in} = 0$, 50, 100, 150, 200, 250, 300, 350 [each profile is separated by a horizontal offset of 0.004. Blue lines, $\overline{\mathrm{Pres.}}_{\rm model}/(\rho_\infty u_\infty^2/\theta_{\rm in})$ (proposed model); circles, $\overline{\mathrm{Pres.}}/(\rho_\infty u_\infty^2/\theta_{\rm in})$ (WRLES database [29])].

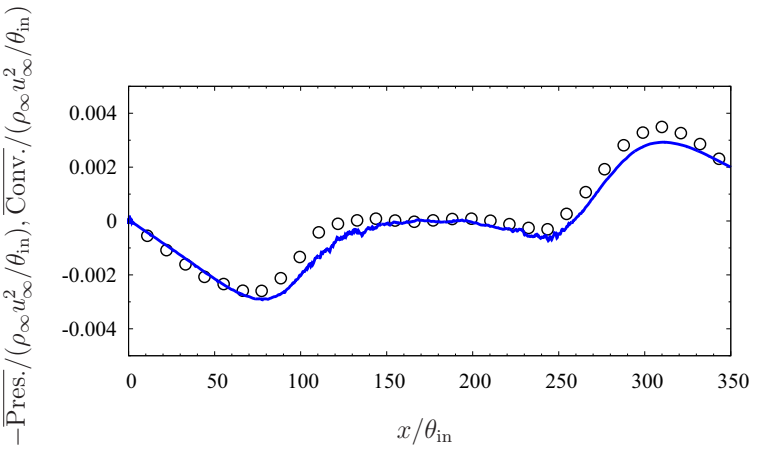

FIG. 5. Convective and pressure-gradient terms at matching location of wall model at $y/\theta_{\text{in}} \approx 0.85$ (approximately 10% of the boundary layer thickness). Blue line, $-\overline{\text{Pres.}}/(\rho_\infty u_\infty^2/\theta_{\text{in}})$; circles, $\overline{\text{Conv.}}/(\rho_\infty u_\infty^2/\theta_{\text{in}})$.

2. Convective term

For the modeling of the convective term [$\overline{\text{Conv.}} = \overline{\rho}\tilde{u}(d\tilde{u}/dx) + \overline{\rho}\tilde{v}(d\tilde{u}/dy)$] in Eq. (4) in the inner layer, we assume that the distributions of the convective term in the inner layer is related to the value of the convective term at the matching location. Therefore, in this study, the convective term is modeled as

$$\overline{\text{Conv.}}_{\text{model}} = \overline{\text{Conv.}}_{\text{model}}\Big|_{h_{\text{wm}}} F(y). \tag{7}$$

Here, the modeling of the convective term is split into two components, the value of the convective term at the matching location h_{wm} and the damping function $F(y)$ to connect between the matching location and the wall.

First, the modeling of $\overline{\text{Conv.}}_{\text{model}}|_{h_{\text{wm}}}$ is considered. Since the matching location locates in the log layer, it is reasonable that the viscous term in Eq. (3) is negligible at the matching location, i.e., $\frac{d}{dy}(\overline{\mu}\frac{d\tilde{u}}{dy})|_{h_{\text{wm}}} \approx 0$. Also, at the matching location within the log layer, we assume that $\frac{d}{dy}(-\overline{\rho}\widetilde{u''v''})|_{h_{\text{wm}}}$ is relatively small compared to the convective and pressure-gradient terms, and thus the convective term and pressure-gradient term are balanced. Therefore, in this study, $\overline{\text{Conv.}}_{\text{model}}|_{h_{\text{wm}}}$ is modeled by using the pressure gradient term at the matching location instead of estimating $\overline{\rho}\tilde{u}d\tilde{u}/dx$ and $\overline{\rho}\tilde{v}d\tilde{u}/dy$ directly as

$$\overline{\text{Conv.}}_{\text{model}}\Big|_{h_{\text{wm}}} = -\left.\frac{d\overline{p}}{dx}\right|_{h_{\text{wm}}}. \tag{8}$$

To validate this modeling, the comparison between the convective and pressure-gradient terms at the height of $y/\theta_{\text{in}} \approx 0.85$ (approximately 10% of the boundary layer thickness) obtained by the WRLES database is shown in Fig. 5. Figure 5 shows that the convective term and pressure-gradient term at the matching location is balanced with each other throughout the separated and reattached regions, indicating the validity of the proposed modeling in Eq (8). We note that Hickel *et al.* [24] also showed the balance between the convective term and the pressure gradient term above the viscous layer in their implicit WRLES of the adverse pressure-gradient turbulent boundary layer [42].

The second component of the convective term modeling in Eq. (7), the damping function $F(y)$, is derived from the original convective term ($\overline{\text{Conv.}} = \overline{\rho}\tilde{u}d\tilde{u}/dx + \overline{\rho}\tilde{v}d\tilde{u}/dy$) by employing the following two assumptions. Since the compressibility effects are generally small in the inner layer of boundary layers, except high-speed flows with a strong wall heat flux, the first assumption is that

the flow compressibility is negligible (i.e., $\partial u_i/\partial x_i \approx 0$, $\tilde{u} \approx \overline{u}$ and $\tilde{v} \approx \overline{v}$) in the inner layer. Using the incompressible continuity equation, the wall-normal velocity in the wall model can be replaced by

$$\tilde{v} \approx \overline{v} = -\int \frac{\partial \overline{u}}{\partial x} dy. \tag{9}$$

The second assumption is that the Favre-averaged streamwise velocity $\tilde{u}$ is expressed as

$$\tilde{u} \approx \overline{u}(x, y) \approx \overline{u}^+(y^+)\, \overline{u_\tau}(x), \tag{10}$$

where we assume that the profile of the nondimensionalized velocity $\overline{u}^+$ is only the function of y^+, while the friction velocity $\overline{u_\tau}$ varies in the streamwise direction x. This assumption suggests that the function form $\overline{u}^+(y^+)$ does not change rapidly in the streamwise direction. Although the applicability to rapidly separated flows should be investigated further in the future, this assumption is essentially valid in the present flow. Substituting Eqs. (9) and (10) into the original convective term ($\overline{\text{Conv.}}$), the convective term can be approximated as

$$\begin{aligned} \overline{\text{Conv.}} &= \overline{\rho}\tilde{u}\frac{\partial \tilde{u}}{\partial x} + \overline{\rho}\tilde{v}\frac{\partial \tilde{u}}{\partial y} \\ &\approx \overline{\rho}\,\overline{u}\frac{\partial \overline{u}^+(y^+)\,\overline{u_\tau}(x)}{\partial x} - \overline{\rho}\left(\int \frac{\partial \overline{u}^+(y^+)\,\overline{u_\tau}(x)}{\partial x} dy\right)\frac{\partial \overline{u}^+(y^+)\,\overline{u_\tau}(x)}{\partial y}. \end{aligned} \tag{11}$$

Here, the derivatives are decomposed by using the chain rule as

$$\begin{aligned} \frac{\partial \overline{u}^+(y^+)\,\overline{u_\tau}(x)}{\partial x} &= \overline{u}^+\frac{d\overline{u_\tau}}{dx} + \overline{u_\tau}\frac{d\overline{u}^+}{dy^+}\frac{\partial y^+}{\partial x} \approx \overline{u}^+\frac{d\overline{u_\tau}}{dx} + \overline{u_\tau}\frac{d\overline{u}^+}{dy^+}\frac{y}{\overline{\nu}_w}\frac{d\overline{u_\tau}}{dx}, \\ &= \overline{u^+}\frac{d\overline{u_\tau}}{dx} + y^+\frac{d\overline{u}^+}{dy^+}\frac{d\overline{u_\tau}}{dx}, \end{aligned} \tag{12}$$

where we assume that $\overline{\nu}_w = \overline{\mu}_w/\overline{\rho}_w$ is approximately constant with respect to x, which is considered to be reasonable under the first assumption (i.e., flow compressibility is negligible in the inner layer). Similarly,

$$\frac{\partial \overline{u}^+(y^+)\overline{u_\tau}(x)}{\partial y} = \overline{u_\tau}\frac{d\overline{u}^+}{dy^+}\frac{dy^+}{dy} = \overline{u_\tau}\frac{\overline{u_\tau}}{\overline{\nu}_w}\frac{d\overline{u}^+}{dy^+}. \tag{13}$$

Substituting Eqs. (12) and (13) into Eq. (11) with the relation $dy = (\overline{\nu}_w/\overline{u_\tau})dy^+$,

$$\begin{aligned} \overline{\text{Conv.}} &\approx \overline{\rho}\,\overline{u}\left(\overline{u}^+\frac{d\overline{u_\tau}}{dx} + y^+\frac{d\overline{u}^+}{dy^+}\frac{d\overline{u_\tau}}{dx}\right) - \overline{\rho}\left[\int\left(\overline{u}^+\frac{d\overline{u_\tau}}{dx} + y^+\frac{d\overline{u}^+}{dy^+}\frac{d\overline{u_\tau}}{dx}\right)dy\right]\frac{\overline{u_\tau}^2}{\overline{\nu}_w}\frac{d\overline{u}^+}{dy^+} \\ &= \overline{\rho}\,\overline{u}\,\overline{u}^+\frac{d\overline{u_\tau}}{dx} + \overline{\rho}\frac{d\overline{u}^+}{dy^+}\frac{d\overline{u_\tau}}{dx}(\overline{u}y^+ - I), \end{aligned} \tag{14}$$

where

$$\begin{aligned} I &= \frac{\overline{u_\tau}^2}{\overline{\nu}_w}\int\left(\overline{u}^+ + \frac{d\overline{u}^+}{dy^+}y^+\right)dy = \overline{u_\tau}\int\left(\overline{u}^+ + \frac{d\overline{u}^+}{dy^+}y^+\right)dy^+ \\ &= \overline{u_\tau}\left(\int \overline{u}^+ dy^+ + \overline{u}^+y^+ - \int \overline{u}^+ dy^+\right) = \overline{u}y^+. \end{aligned} \tag{15}$$

Finally, by substituting Eq. (15) into Eq. (14), the convective term can be approximated as

$$\overline{\text{Conv.}} \approx \overline{\rho}\,\overline{u}\,\overline{u}^+\frac{d\overline{u_\tau}}{dx} = \overline{\rho}\,\overline{u}^2\frac{1}{\overline{u_\tau}}\frac{d\overline{u_\tau}}{dx} \propto \overline{\rho}\,\overline{u}^2, \tag{16}$$

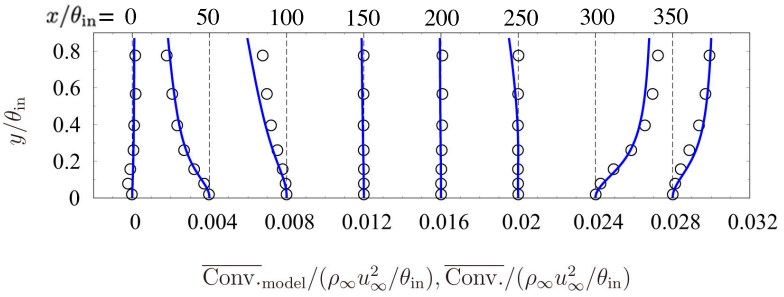

FIG. 6. *A priori* test of the proposed modeling of the convective term at $x/\theta_{\rm in} = 0$, 50, 100, 150, 200, 250, 300, 350 [each profile is separated by a horizontal offset of 0.004. Blue lines, $\overline{\rm Conv.}_{\rm model}/(\rho_\infty u_\infty^2/\theta_{\rm in})$ (proposed model); circles, $\overline{\rm Conv.}/(\rho_\infty u_\infty^2/\theta_{\rm in})$ (WRLES database [29])].

where since $(1/\overline{u}_\tau)(d\overline{u}_\tau/dx)$ is constant in wall-normal direction, the wall-normal distributions of $\overline{\rm Conv.}$ become proportional to $\overline{\rho}\,\overline{u}^2$. Based on the analysis, we propose to model the wall-normal damping function of the convective term as

$$F(y) = \frac{\overline{\rho}\,\overline{u}^2}{(\overline{\rho}\,\overline{u}^2)|_{h_{\rm wm}}}, \tag{17}$$

where $(\overline{\rho}\,\overline{u}^2)|_{h_{\rm wm}}$ is the $\overline{\rho}\,\overline{u}^2$ at the matching location $h_{\rm wm}$.

Consequently, the proposed modeling of the convective term is represented as

$$\overline{\rm Conv.}_{\rm model} = -\left.\frac{d\overline{p}}{dx}\right|_{h_{\rm wm}} \frac{\overline{\rho}\,\overline{u}^2}{(\overline{\rho}\,\overline{u}^2)|_{h_{\rm wm}}}. \tag{18}$$

Note that the convective term modeled by Hickel *et al.* [24] is

$$\tilde{u}_j \frac{\partial \tilde{u}}{\partial x_j} \approx \left(\tilde{u}_j \frac{\partial \tilde{u}}{\partial x_j}\right)\bigg|_{h_{\rm wm}} \left|\frac{\tilde{u}}{\tilde{u}|_{h_{\rm wm}}}\right|^\alpha, \tag{19}$$

where the free parameter α of the damping function is determined to fit their implicit WRLES database and set to $\alpha = 1.5$. In this study, we analytically derive the damping function $F(y)$ by the analysis of the convective term, which suggests $F(y) \propto \overline{\rho}\,\overline{u}^2$ (in other words, under the assumption of constant density, our study indicates $\alpha = 2.0$).

Similar to the pressure-gradient term, the proposed convective-term modeling of Eq. (18) is validated through *a priori* tests using the WRLES database. Figure 6 compares the proposed model and the WRLES database of $\overline{\rm Conv.} = \overline{\rho}\tilde{u}d\tilde{u}/dx + \overline{\rho}\tilde{v}d\tilde{u}/dy$ at the streamwise locations $x/\theta_{\rm in} = 0$, 50, 100, 150, 200, 250, 300, 350. The proposed model reasonably well predicts the convective-term profiles obtained by the WRLES database throughout the separated and reattached regions, indicating the validity of the proposed convective-term modeling.

3. Turbulent eddy viscosity

In the existing PDE-based [10,11,13,14] and ODE-based [24] NEQBL models, the turbulent eddy viscosity used in the wall model is calculated by the typical mixing length model,

$$\overline{\mu}_{t,\rm eq} = \overline{\rho}\kappa y \sqrt{\frac{|\overline{\tau}_w|}{\overline{\rho}}} D^+, \tag{20}$$

where the wall-damping function is

$$D^+ = \left[1 - \exp\left(-\frac{y^+}{A}\right)\right]^2. \tag{21}$$

In this model, the mixing length l is assumed to be proportional to the distance from the wall (i.e., $l \approx \kappa y$), and the turbulent eddy viscosity is damped in terms of y^+ near the wall by the wall-damping function D^+.

In the mixing length model, Reynolds shear stress is expressed as

$$-\overline{\rho}\widetilde{u''v''} = \overline{\mu}_t \frac{d\overline{u}}{dy} = \overline{\rho} l^2 \left|\frac{d\overline{u}}{dy}\right| \frac{d\overline{u}}{dy}. \tag{22}$$

In the log layer, since the viscous term is negligible, the total shear stress $\overline{\tau}$ of the equilibrium boundary layers becomes

$$\overline{\tau} = \overline{\tau}_w = \overline{\mu}\frac{d\overline{u}}{dy} - \overline{\rho}\widetilde{u''v''} \approx -\overline{\rho}\widetilde{u''v''}. \tag{23}$$

Substituting Eq. (22) into Eq. (23) yields

$$\sqrt{\frac{|\overline{\tau}|}{\overline{\rho}}} \approx l\left|\frac{d\overline{u}}{dy}\right|. \tag{24}$$

Furthermore, by substituting Eq. (24) into Eq. (22), the turbulent eddy viscosity can be formulated as

$$\overline{\mu}_t = \overline{\rho} l \sqrt{\frac{|\overline{\tau}|}{\overline{\rho}}} = \overline{\rho}\kappa y \sqrt{\frac{|\overline{\tau}|}{\overline{\rho}}}. \tag{25}$$

In the equilibrium boundary layers where the total shear stress $\overline{\tau}$ is equal to the wall shear-stress $\overline{\tau}_w$ as in Eq. (23), Eq. (25) is identical to Eq. (20) except for the wall damping.

The issue here is that the equilibrium boundary-layer assumption is inaccurate in the nonequilibrium boundary layers where the pressure-gradient and convective terms are not negligible. Therefore, the turbulent eddy viscosity also needs to take the nonequilibrium effects into account in the formulation in addition to modeling the pressure-gradient and convective terms themselves. In the nonequilibrium boundary layers, the total shear stress $\overline{\tau}$ in the log layer becomes

$$\overline{\tau} = \overline{\tau}_w + \int (\overline{\text{Conv.}} + \overline{\text{Pres.}})dy, \tag{26}$$

that can be derived from the streamwise momentum equation Eq. (3) where the thin-layer approximation is applied.

In this study, therefore, we propose to model the turbulent eddy viscosity by using the total shear stress that includes the nonequilibrium effects. From the conservation of the streamwise momentum, $\overline{\tau}_{\text{model}}$ is computed as

$$\overline{\tau}_{\text{model}} = \overline{\tau}_w + \int (\overline{\text{Conv.}}_{\text{model}} + \overline{\text{Pres.}}_{\text{model}})dy. \tag{27}$$

Consequently, we propose to model the turbulent eddy viscosity as

$$\overline{\mu}_{t,\text{model}} = \overline{\rho}\kappa y \sqrt{\frac{|\overline{\tau}_{\text{model}}|}{\overline{\rho}}} D^*, \tag{28}$$

where

$$D^* = \left[1 - \exp\left(-\frac{y^*}{A}\right)\right]^2, \tag{29}$$

with

$$y^* = y\frac{\overline{u}^*_\tau}{\overline{\nu}_w}, \quad \overline{u}^*_\tau = \sqrt{\frac{|\overline{\tau}_{\text{model}}|}{\overline{\rho}_w}}. \tag{30}$$

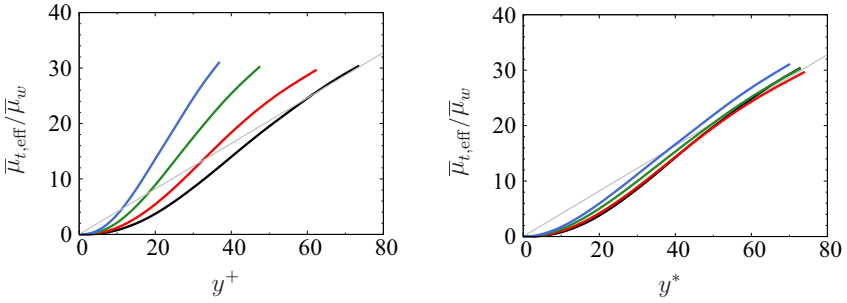

(a) Typical y^+ scaling (b) Proposed y^* scaling

FIG. 7. Effective turbulent eddy viscosity under the adverse pressure gradient obtained by WRLES database [29]. Black lines, $x/\theta_{\mathrm{in}} = 0$; red lines, $x/\theta_{\mathrm{in}} = 50$; green lines, $x/\theta_{\mathrm{in}} = 75$; blue lines, $x/\theta_{\mathrm{in}} = 87.5$; gray lines, $\overline{\mu}_{t,\mathrm{eff}}/\mu_w = \kappa y^+$ in (a) and $\overline{\mu}_{t,\mathrm{eff}}/\mu_\infty = \kappa y^*$ in (b) where $\kappa = 0.41$.

In this model, the turbulent eddy viscosity is damped in terms of y^* with the wall-damping function D^* instead of using y^+, which also includes the nonequilibrium effects. Naturally, in the equilibrium boundary layers where $\overline{\tau} = \overline{\tau}_w$, the proposed turbulent eddy viscosity model Eq. (28) reduces to Eq. (20).

The validity of Eq. (28) is investigated by comparing the proposed turbulent eddy viscosity model [Eq. (28)] that incorporates the nonequilibrium effects into the model with the widely used eddy viscosity model [Eq. (20)]. In the validation, the effective turbulent eddy viscosity $\overline{\mu}_{t,\mathrm{eff}} = -\overline{\rho}\widetilde{u''v''}/(d\overline{u}/dy)$ that is calculated by the WRLES database is used. A simple variation of Eq. (28) with the use of $\overline{\rho} \approx \overline{\rho}_w$ leads to $\overline{\mu}_{t,\mathrm{model}}/\overline{\mu}_w \approx \kappa y^* D^*$, which suggests that $\overline{\mu}_{t,\mathrm{model}}/\overline{\mu}_w \approx \kappa y^*$ in the logarithmic region. Similarly, from Eq. (20), $\overline{\mu}_{t,\mathrm{eq}}/\overline{\mu}_w \approx \kappa y^+ D^+$. Figure 7 shows the effective turbulent eddy viscosity $\overline{\mu}_{t,\mathrm{eff}}/\overline{\mu}_w$ obtained by the WRLES database at the adverse pressure-gradient region ($x/\theta_{\mathrm{in}} = 0$, 50, 75, 87.5) in terms of the typical wall unit y^+ ($= y\overline{u}_\tau/\overline{\nu}_w$) and the proposed wall scaling y^* ($= y\overline{u}^*_\tau/\overline{\nu}_w$) to validate the proposed turbulent eddy viscosity model [Eq. (28)]. The effective turbulent eddy viscosity in the proposed y^* scaling collapses well to the κy^* line in the logarithmic region, while the profiles are scattered with the typical y^+ scaling. The WRLES data indicate the validity of the proposed turbulent eddy viscosity model [Eq. (28)] scaling with y^* (as suggested in Appendix, by incorporating the effects of pressure gradient into the wall-damping function, the collapse of the turbulent eddy viscosity may further improve).

The proposed modeling of the turbulent eddy viscosity in Eq. (28) is also validated through *a priori* tests using the WRLES database. Figure 8 compares the proposed model [Eq. (28)],

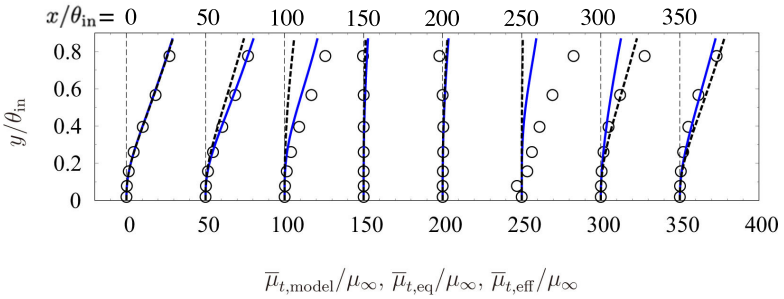

FIG. 8. *A priori* test of the proposed modeling of the turbulent eddy viscosity at $x/\theta_{\mathrm{in}} = 0$, 50, 100, 150, 200, 250, 300, 350 (each profile is separated by a horizontal offset of 50). Blue lines, $\overline{\mu}_{t,\mathrm{model}}/\mu_\infty$ (proposed model); black dashed lines, $\overline{\mu}_{t,\mathrm{eq}}/\mu_\infty$ (existing model); circles, $\overline{\mu}_{t,\mathrm{eff}}/\mu_\infty$ (WRLES database [29]).

the existing eddy-viscosity model [Eq. (20)], and the reference effective turbulent eddy viscosity $\overline{\mu}_{t,\mathrm{eff}} = -\overline{\rho}\widetilde{u''v''}/(d\overline{u}/dy)$ obtained by the WRLES database at the streamwise locations $x/\theta_{\mathrm{in}} =$ 0, 50, 100, 150, 200, 250, 300, 350. In both the eddy viscosity models, κ and A are set to 0.41 and 17 as followed by the prior study [12]. In the attached equilibrium turbulent-boundary-layer region at the inlet $x/\theta_{\mathrm{in}} = 0$, the two models [Eqs. (28) and (20)] show almost identical results. The results indicate that the proposed model automatically reduces to the typical equilibrium model when the nonequilibrium effects are negligible (i.e., $\overline{\tau} \approx \overline{\tau}_w$). In the separated region under the adverse pressure gradient ($x/\theta_{\mathrm{in}} = 50, 100$) where the nonequilibrium effects are not negligible, the proposed turbulent-eddy-viscosity model shows superior predictions compared to the existing model, indicating the validity of including the nonequilibrium effects in the eddy-viscosity model. In the boundary layer downstream of of the reattachment ($x/\theta_{\mathrm{in}} = 250, 300, 350$), the proposed model shows a certain deviation from the WRLES database. The root of the deviation is considered to be caused by the framework of the mixing length model itself. In the mixing length model, the turbulence scale is assumed to be proportional to the single length scale, the distance from the wall (i.e., $l \approx \kappa y$), and the proportional coefficient is calibrated by the equilibrium fully developed turbulent boundary layers. In the boundary layer downstream of the reattachment, however, the lifted large-scale turbulent structures that grew in the separated shear-layer flow down and merge with the boundary layer as discussed by Abe [31] (also observed by the present WRLES shown in the reattached downstream region in Fig. 1). Therefore, the mixing length l is not considered to be only the function of y, i.e., $l \neq \kappa y$ in the reattached region. Also, at $x/\theta_{\mathrm{in}} = 350$, the boundary layer is still spatially developing after the reattachment. As a result, we conclude that the discrepancies in the proposed model after the reattachment is due to the invalidity of $l \approx \kappa y$ employed by the mixing length model.

C. Implementation of the proposed ODE-based NEQBL wall model

The proposed ODE-based nonequilibrium wall-model equation, which is solved in an overlapping layer between the wall $y = 0$ and the matching location $y = h_{\mathrm{wm}}$ with the adiabatic (or isothermal) no-slip boundary condition at the wall, is

$$\frac{d}{dy}\left[(\mu + \mu_{t,\mathrm{model}})\frac{du}{dy}\right] = \mathrm{Conv.}_{\mathrm{model}} + \mathrm{Pres.}_{\mathrm{model}}. \tag{31}$$

Based on the proposed modeling of nonequilibrium effects discussed in Sec. II B, the modeled nonequilibrium terms are implemented as

$$\begin{aligned}
\mathrm{Pres.}_{\mathrm{model}} &= \left\langle \frac{dp}{dx} \right\rangle\Big|_{h_{\mathrm{wm}}}, \\
\mathrm{Conv.}_{\mathrm{model}} &= -\left\langle \frac{dp}{dx} \right\rangle\Big|_{h_{\mathrm{wm}}} \min\left(\frac{\rho u^2}{(\rho u^2)|_{h_{\mathrm{wm}}} + \epsilon}, 1\right), \\
\mu_{t,\mathrm{model}} &= \rho\kappa y\sqrt{\frac{|\tau_{\mathrm{model}}|}{\rho}}\left[1 - \exp\left(-\frac{y^*}{A}\right)\right]^2,
\end{aligned} \tag{32}$$

where

$$\begin{aligned}
y^* &= y\frac{u^*_{\tau\,\mathrm{model}}}{\nu_w},\ u^*_{\tau\,\mathrm{model}} = \sqrt{\frac{|\tau_{\mathrm{model}}|}{\rho_w}}, \\
\tau_{\mathrm{model}} &= \tau_w + \left\langle \frac{dp}{dx} \right\rangle\Big|_{h_{\mathrm{wm}}} \cdot y + \int_0^y \mathrm{Conv.}_{\mathrm{model}}\, dy.
\end{aligned} \tag{33}$$

$\epsilon = 1 \times 10^{-12}$ is the small positive constant to prevent division by zero, and the convective term is clipped by a value at the matching location to assure the convergence of the wall-model solution in

the region where the streamwise velocity at the matching location is too small. Here, u is the solution of the wall model itself. Since the velocity generally decreases from the matching height to the wall, we assume that the function $\rho u^2/(\rho u^2)|_{h_{wm}}$ does not exceed one except in the particular case near the separation point. Note that the top boundary conditions at $y = h_{\rm wm}$ for the wall-model equation are imposed by the instantaneous LES solutions of ρ, u, p at the matching location similar to the prior wall model studies [12,13], while dp/dx is replaced with an averaged quantity $\langle dp/dx\rangle$ to stabilize the wall-model calculation. In this study, $\langle\ \rangle$ denotes the averaged quantity in the homogeneous spanwise direction, and κ and A are set to 0.41 and 17. Note that in a practical 3D flow simulations, the x axis should be taken in the local flow direction at the matching height. Also, the averaging in the homogeneous direction $\langle\ \rangle$ may be replaced by a low-pass spatial filtering or exponential moving average.

D. Summary of modeling assumptions

Here, we list the modeling assumptions employed in the proposed model. First, the fundamental assumptions are

(1) The inner-layer flow follows the thin-layer assumption [Eq. (3)].

(2) The convection and pressure-gradient terms balance at the matching height $y = h_{\rm wm}$ at the log layer [Eq. (8)].

The modeling of the pressure-gradient term assumes

(3) The pressure is constant in the wall-normal direction below the matching location, and thus the streamwise pressure gradient is constant in the wall-normal direction [Eq. (6)].

Furthermore, the modeling of the convection term employs the following assumptions

(4) In the near-wall region, the flow compressibility is negligible [Eq. (9)].

(5) The mean velocity profile may be split into $\tilde{u}(x, y) \approx \overline{u}^+(y^+)\overline{u_\tau}(x)$ [Eq. (10)].

Finally, the modeling of the eddy viscosity assumes

(6) The eddy viscosity is given by the mixing-length model using the local total shear stress [Eq. (25)].

Among the assumptions above, 1, 2, and 3 are employed also by Hickel *et al.* [24], while 4, 5, and 6 are the originals of this study. Although it depends on the contribution each assumption makes to the modeling, it is possible that the model may not work well for flows that do not match the modeling assumptions.

III. *A PRIORI* ANALYSES OF THE PROPOSED ODE-BASED NEQBL WALL MODEL

To validate the proposed wall model [Eq. (31)], the skin friction, which is used for the wall flux boundary condition in the WMLES, obtained by solving Eq. (31) is compared with the WRLES database through *a priori* tests using the WRLES data. In addition to the proposed wall model Eq. (31), the following models are also examined to show the importance of consistently modeling the three terms (i.e., the pressure-gradient term, convective term, and turbulent eddy viscosity) to incorporate the nonequilibrium effects properly.

$$\text{Model A: } \frac{d}{dy}\left[(\overline{\mu}+\overline{\mu}_{t,\rm eq})\frac{d\overline{u}}{dy}\right] = \overline{\text{Pres.}}_{\rm model},$$

$$\text{Model B: } \frac{d}{dy}\left[(\overline{\mu}+\overline{\mu}_{t,\rm eq})\frac{d\overline{u}}{dy}\right] = \overline{\text{Conv.}}_{\rm model},$$

$$\text{Model C: } \frac{d}{dy}\left[(\overline{\mu}+\overline{\mu}_{t,\rm model})\frac{d\overline{u}}{dy}\right] = 0,$$

$$\text{Model D: } \frac{d}{dy}\left[(\overline{\mu}+\overline{\mu}_{t,\rm eq})\frac{d\overline{u}}{dy}\right] = \overline{\text{Pres.}}_{\rm model} + \overline{\text{Conv.}}_{\rm model},$$

$$\text{Model E: } \frac{d}{dy}\left[(\overline{\mu}+\overline{\mu}_{t,\text{model}})\frac{d\overline{u}}{dy}\right]=\overline{\text{Pres.}}_{\text{model}},$$

$$\text{Model F: } \frac{d}{dy}\left[(\overline{\mu}+\overline{\mu}_{t,\text{model}})\frac{d\overline{u}}{dy}\right]=\overline{\text{Conv.}}_{\text{model}}.$$

Models A, B, and C include one of the nonequilibrium effects (i.e., $\overline{\text{Pres.}}_{\text{model}}$ in Model A, $\overline{\text{Conv.}}_{\text{model}}$ in Model B, and $\overline{\mu}_{t,\text{model}}$ in Model C), while the other two nonequilibrium effects are not incorporated. Models D, E, and F include two of the nonequilibrium effects, while the remaining one term is not modeled. Here, the modeled terms $\overline{\text{Pres.}}_{\text{model}}$, $\overline{\text{Conv.}}_{\text{model}}$, and $\overline{\mu}_{t,\text{model}}$ are calculated by Eqs. (6), (18), and (28), respectively, and $\overline{\mu}_{t,\text{eq}}$ is calculated by Eq. (20).

Figure 9 compares the skin friction $C_f \equiv 2\overline{\tau}_w/(\rho_\infty u_\infty^2)$ predicted by each model. Here, the result obtained by the EQBL model [12] (i.e., $\frac{d}{dy}[(\overline{\mu}+\overline{\mu}_{t,\text{eq}})\frac{d\overline{u}}{dy}]=0$) is also included. The proposed model shows an overall good agreement with the WRLES database except for the small deviation from the WRLES database downstream of the reattachment at $x/\theta_{\text{in}} \gtrsim 300$. However, the models that do not consistently model the three nonequilibrium effects (Model A–F) show large deviations from the WRLES database. For example, Model D (the model that includes the pressure-gradient and convective terms without modifying the turbulent eddy viscosity) predicts the flow separation far upstream. The result of Model D indicates the significant importance of reflecting the nonequilibrium effects in the turbulent eddy viscosity modeling in addition to the modeling of the pressure-gradient and convective terms, which has not been discussed in prior studies. That is, the model that neglects any one of the nonequilibrium effects is inaccurate. These results indicate the importance of consistently incorporating the nonequilibrium effects into all of the pressure-gradient term, convective term, and turbulent eddy viscosity. Note that although there is a discrepancy in the reattached region, the EQBL model reasonably accurately predicts the skin friction coefficient upstream of the flow separation. However, this reasonable prediction in the upstream of the flow separation does not indicate the validity of the EQBL model because all the terms (i.e., $\overline{\text{Pres.}}_{\text{model}}$, $\overline{\text{Conv.}}_{\text{model}}$, and $\overline{\mu}_{t,\text{model}}$) are inconsistent with the WRLES. Such inconsistency may cause the dependency of the results on flow conditions or matching height.

Furthermore, we investigate the cause of the discrepancy downstream of the reattachment at $x/\theta_{\text{in}} \gtrsim 300$ obtained by the proposed model, since this discrepancy may influence the development of the boundary layers downstream of the reattachment. Figure 10 shows a skin friction obtained by solving following equation:

$$\frac{d}{dy}\left[(\overline{\mu}+\overline{\mu}_{t,\text{eff}})\frac{d\overline{u}}{dy}\right]=\overline{\text{Pres.}}_{\text{model}}+\overline{\text{Conv.}}_{\text{model}}, \tag{34}$$

where $\overline{\mu}_{t,\text{eff}} = -\overline{\rho}\widetilde{u''v''}/(d\overline{u}/dy)$ is the effective eddy viscosity calculated by using the WRLES database, while the right-hand side modeling is retained from Model D. Using the effective eddy viscosity (i.e., using the correct eddy viscosity obtained by the WRLES database), the model prediction is improved in the regions downstream of the reattachment. The result indicates that the modeling of the turbulent eddy viscosity is the key to improving the prediction of skin friction in the reattached regions. Note that as discussed in Sec. II B 3, in the reattached region, the separated shear layer with the large-scale turbulent structures flows down and merges to the reattached turbulent boundary layer, indicating that the mixing length l is not considered to be only the function of y, i.e., $l \neq \kappa y$ as typically used, in the reattached region. This fact makes the turbulent-eddy-viscosity modeling at the reattachment region challenging.

IV. NUMERICAL EXPERIMENTS

In this section, the proposed ODE-based NEQBL wall model is implemented to the solver, and the LES with the proposed model [Eqs. (31) and (32)] is conducted for the flat-plate zero-pressure-gradient and separated turbulent boundary layers to investigate the behavior of the proposed

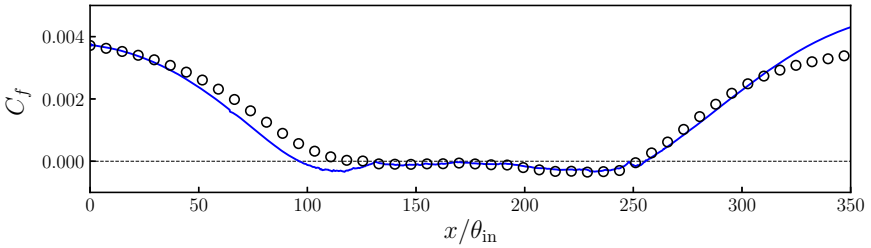

(a) Proposed model. Blue line, the proposed model; circles, WRLES database[29]

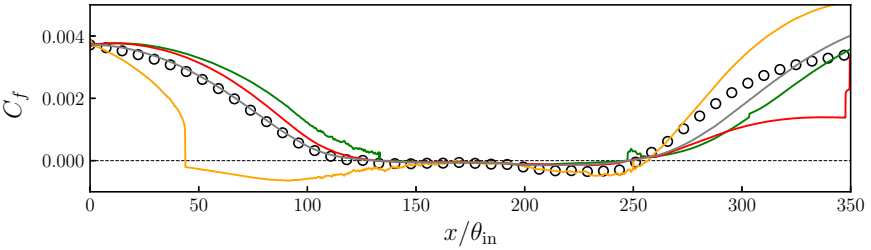

(b) Models including zero or only one of the non-equilibrium effects. Orange line, Model A; green line, Model B; red line, Model C; grey line, EQBL model, circles, WRLES database[29]

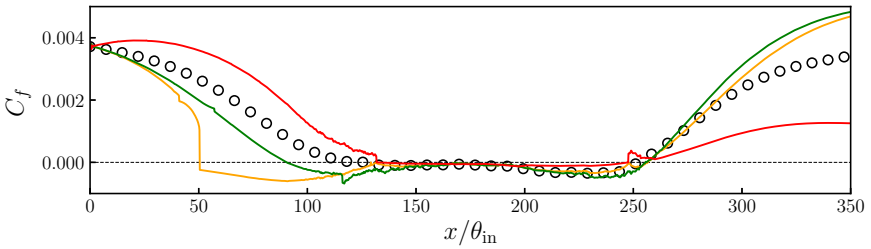

(c) Models including only two of the non-equilibrium effects. Orange line, Model D; green line, Model E; red line, Model F; circles, WRLES database[29]

FIG. 9. Skin friction coefficient C_f predicted by *a priori* test of various wall models.

wall-model implemented in the LES. The flow conditions and the computational domain size are the same as the WRLES database described in Sec. II A. The turbulent boundary layer of the driver section is under the zero pressure gradient and is used for the inflow conditions in the test section shown in Fig. 1. In the test section, the fully developed attached turbulent boundary layer separates in the adverse pressure-gradient region and then reattaches in the favorable-pressure-gradient region. The results are compared to those obtained by the existing PDE-based NEQBL wall model [13] and the WRLES database. The streamwise and spanwise grid spacings are $\Delta x = \Delta z \approx \delta_{\rm in}/25$ (where $\delta_{\rm in}$ is the boundary layer thickness at the inlet of the test section), and the wall-normal grid spacing is $\Delta y_w \approx \delta_{\rm in}/100$ near the wall and $\Delta y \approx \delta_{\rm in}/25$ at the height of the outer layer. Here, 48 and 57 grid points exist below the inflow boundary layer thickness in the test section and the height of

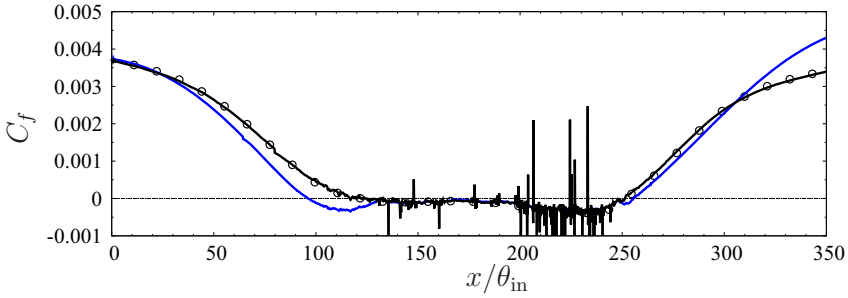

FIG. 10. Skin friction coefficient C_f predicted by *a priori* test of wall model. Blue line, the proposed ODE-based wall model with turbulent eddy viscosity $\overline{\mu}_{t,\rm model}$ (Eq. (28)); black line, the proposed ODE-based wall model with effective turbulent eddy viscosity $\overline{\mu}_{t,\rm eff}$; circles, WRLES database [29].

the recirculation region, respectively. Also, the matching point is the tenth grid point from the wall ($y/\delta_{\rm in} = 0.10$). Our prior WMLES study [12] indicates that the employed grid spacing is sufficient to achieve the grid convergence of statistics using the sixth-order compact differencing scheme [38]. The total number of grid points is about 90 million, which is 18 times smaller than that of the WRLES. In addition to the LES grid, the 1D grid for solving the ODE-based wall model has 43 points between the wall and matching height, where the grid spacing at the wall satisfies $\Delta y_w^+ < 1$. The wall-normal resolution of the ODE grid is comparable to the WRLES, which sufficiently resolves the mean flow variables in the viscous sub-layer and the buffer layer. Also, the time-step size can be increased from the WRLES the large Δy_w. Here, we set the time step size to $\Delta t u_\infty/\delta_{\rm in} \approx 1.2 \times 10^{-3}$, which is 6 times larger than that of the WRLES ($\Delta t u_\infty/\delta_{\rm in} \approx 2.0 \times 10^{-4}$). Note that the ODE-based model does not restrict the time step size even though the grid spacing within the ODE is small. The employed numerical methods are the same as the WRLES described in Sec. II A. The spatial derivatives and the time advancement are evaluated by using the sixth-order compact difference scheme [38] and the third-order total variation diminishing Runge-Kutta method [40], respectively. The SGS turbulent eddy viscosity is calculated by the selective mixed-scale model [41]. After the flow reaches a quasi-steady state, the turbulence statistics are computed by averaging in time for a time interval of $9600\theta_{\rm in}/u_\infty$ and in the homogeneous spanwise direction to ensure convergence of flow statistics.

A. Zero-pressure-gradient attached turbulent boundary layer

The turbulent statistics of the zero-pressure-gradient attached turbulent boundary layer in the driver section are shown in Fig. 11. Figure 11(a) shows the streamwise evolution of the skin friction, and Figs. 11(b) and 11(c) show the mean streamwise velocity and Reynolds stresses at $\mathrm{Re}_\theta \approx 2.0 \times 10^3$, respectively. The skin friction developments obtained by both the proposed ODE-based and existing PDE-based NEQBL wall models show a good agreement with the WRLES database, and all the results are within 5% differences from the correlation proposed by Schlichting [43]. The mean velocity profiles reasonably follow the log-law, and the Reynolds stresses obtained by both the ODE-based and PDE-based NEQBL models also show a good agreement with the WRLES database.

B. Pressure-gradient-induced separated and reattached flat-plate turbulent boundary layer

The WMLES results of the mean streamwise velocity and Reynolds shear stress are compared in Figs. 12 and 13. Both the mean streamwise velocity and Reynolds shear stress predicted by the proposed ODE-based NEQBL wall model agree reasonably well with the corresponding WRLES database. Also, the predicted results are almost identical to the results obtained by the existing PDE-based NEQBL model [13], in which time-dependent partial differential equations are solved.

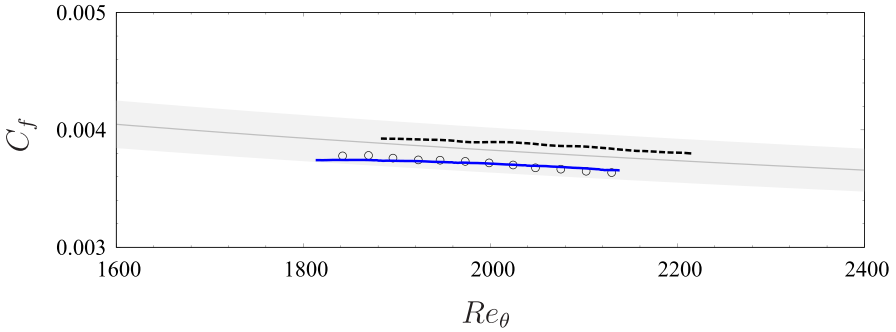

(a) Skin friction evolution in terms of Reynolds number based on momentum thickness

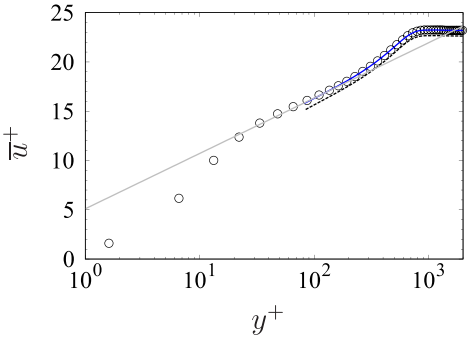

(b) Mean streamwise velocity at $Re_\theta \approx 2000$

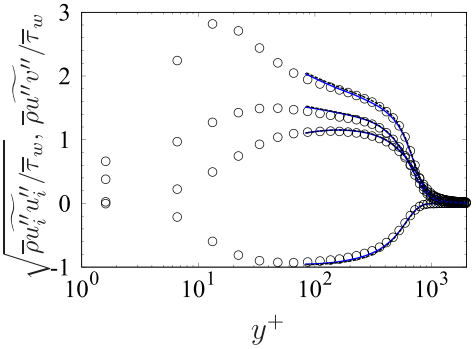

(c) Reynolds stresses at $Re_\theta \approx 2000$: upper, $\sqrt{\overline{\rho}\widetilde{u''u''}/\overline{\tau}_w}$; upper-middle, $\sqrt{\overline{\rho}\widetilde{w''w''}/\overline{\tau}_w}$; lower-middle, $\sqrt{\overline{\rho}\widetilde{v''v''}/\overline{\tau}_w}$; lower, $\overline{\rho}\widetilde{u''v''}/\overline{\tau}_w$

FIG. 11. Turbulent statistics of the zero-pressure-gradient turbulent boundary layer. Blue lines, proposed ODE-NEQBL wall model; black dashed-lines, PDE-NEQBL wall model [13]; circles, WRLES database [29]; gray line in (a), Schlichting[43] (shaded regions are ±5%); gray line in (b), $\overline{u}^+ = 1/0.41\log(y^+) + 5.2$.

Next, the modeled nonequilibrium effects are validated term-by-term by directly comparing with the corresponding WRLES database at the streamwise locations ($x/\theta_{\text{in}} = 0$, 50, 100, 150, 200, 250, 300, and 350). The pressure-gradient term, convective term, and turbulent eddy viscosity obtained by the proposed ODE-based NEQBL wall model at $0 \leqslant y \leqslant h_{\text{wm}}$ are compared with the near-wall WRLES database in Fig. 14. The proposed ODE-based NEQBL model reasonably well predicts the nonequilibrium terms and the turbulent eddy viscosity, similar to the *a priori* tests discussed in Sec. II. The results suggests that the proposed model works reasonably well in the separated and reattached turbulent boundary layer, even if the instantaneous LES solutions are used as the input for the wall model instead of using the averaged data as in the *a priori* tests.

Finally, the skin friction and wall pressure obtained by the proposed ODE-based and existing PDE-based NEQBL wall models are compared with the WRLES database in Fig. 15. In the WMLES, the predicted skin friction (i.e., wall-shear stress τ_w) is fed back to the LES as a flux boundary condition. In the adverse pressure-gradient region prior to the separation ($x/\theta_{\text{in}} \lesssim 100$), the proposed ODE-based NEQBL model predicts the skin friction slightly better than the existing PDE-based NEQBL model. The improvement in the proposed ODE-based NEQBL model is mainly due to the proposed turbulent eddy viscosity modeling that incorporates the nonequilibrium effects of the pressure-gradient and convective terms consistently into the model. In the separation bubble ($100 \lesssim x/\theta_{\text{in}} \lesssim 250$), overall the proposed ODE-based NEQBL model predicts the skin

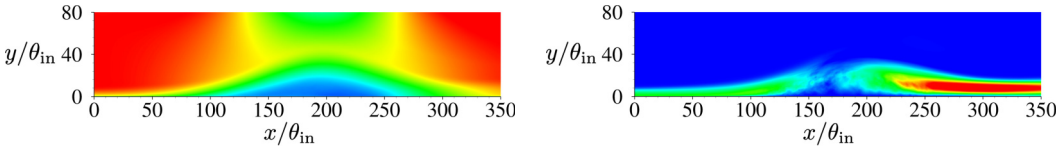

(a) WRLES database[29]

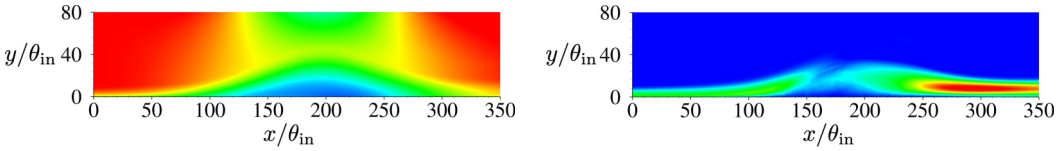

(b) Proposed ODE-based NEQBL wall model

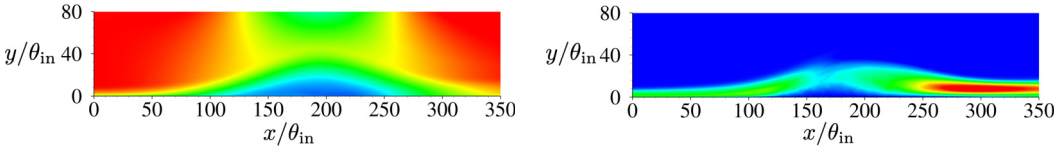

(c) PDE-based NEQBL wall model[13]

FIG. 12. Mean streamwise velocity $\tilde{u}/u_\infty$ (left) and Reynolds shear stress $-\overline{\rho}\widetilde{u''v''}/(\rho_\infty u_\infty^2)$ (right).

friction reasonably well. However, the proposed model does not reproduce the negative C_f dip at $200 \lesssim x/\theta_{\rm in} \lesssim 250$. Since the negative C_f dip is successfully predicted in the *a priori* test (see Fig. 9), the slight deterioration in the predicted C_f may be due to the use of instantaneous LES solutions as an input of the wall model, while the averaged LES solutions are used as an input of the wall model in the *a priori* tests. The result also suggests that the fluctuation components are not negligible in this region. We note that as Tamaki *et al.* [19] indicated, this slight deterioration in the C_f prediction obtained by the proposed ODE-based NEQBL model is considered not to significantly affect the LES solution because the small skin friction in the separated region has little effect on the boundary layer development [19]. In the favorable-pressure-gradient region downstream of the reattachment ($x/\theta_{\rm in} \gtrsim 250$), both the ODE-based and PDE-based NEQBL models show a deviation from the WRLES database. We consider that the deviation is due to the failure of the mixing length model in the reattached region, as discussed in Sec. III (see also Fig. 10).

V. CONCLUSIONS

In this study, we proposed an ODE-based nonequilibrium boundary layer (NEQBL) wall model that does not require a computational grid with full connectivity for accurately predicting separated nonequilibrium turbulent boundary layers. In the proposed modeling, the nonequilibrium effects, i.e., the pressure-gradient term, convective term, and turbulent eddy viscosity, were consistently

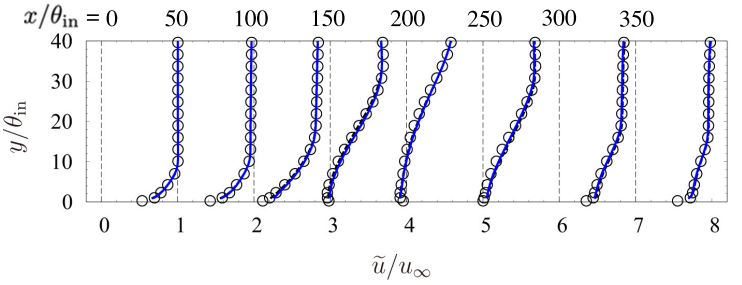

(a) Mean streamwise velocity (each profile is separated by a horizontal offset of 1.0)

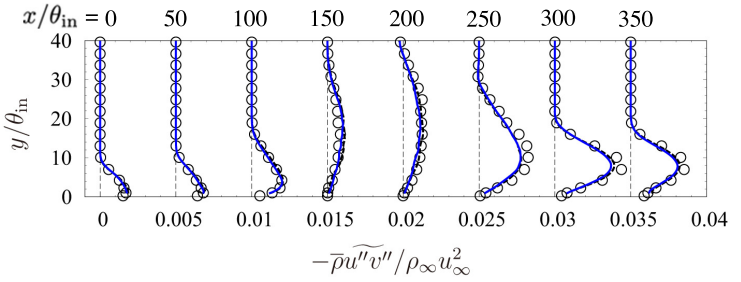

(b) Reynolds shear stress (each profile is separated by a horizontal offset of 0.005)

FIG. 13. Mean streamwise velocity and Reynolds shear stress at streamwise locations $x/\theta_{in} = 0$, 50, 100, 150, 200, 250, 300, 350. Blue lines, proposed ODE-based NEQBL wall model; black dashed-lines, PDE-based NEQBL wall model [13]; circles, WRLES database [29].

modeled term-by-term and first validated through *a priori* tests using the WRLES database of the pressure-gradient-induced separated and reattached flat-plate turbulent boundary layer at Reynolds number $\mathrm{Re}_\theta \approx 2.0 \times 10^3$. Then, the WMLES using the proposed ODE-based NEQBL model was conducted under the same condition as the WRLES database and validated by comparing the results with the WRLES database and the existing PDE-based NEQBL model.

The key to the modeling is to incorporate the nonequilibrium effects into the pressure-gradient term, convective term, and turbulent eddy viscosity consistently. The model that does not consistently model any of these terms is inaccurate. Also, it was found the significant importance of reflecting the nonequilibrium effects into the turbulent eddy viscosity, which has not been discussed in prior studies. The turbulent eddy viscosity is modeled using the total shear stress, including the nonequilibrium effects of the pressure-gradient and convective terms, while the existing turbulent eddy viscosity model assumes the equilibrium boundary layer. The proposed convective term modeling comprises the value at the matching location and wall damping function. A simple analysis of the turbulent statistics within the inner layer leads to the value of the convective term at the matching location, which is equivalent to the pressure gradient term, i.e., the convective term and pressure-gradient term at the matching location are balanced. The wall-damping function of the convective term is then analytically derived with two assumptions summarized in Sec. II D, which does not include any tuning parameters.

The *a priori* tests using the WRLES database showed the validity of each modeling term and the importance of consistency among the pressure-gradient term, convective term, and turbulent eddy viscosity. The WMLES using the proposed ODE-based NEQBL wall model predicts the mean streamwise velocity and Reynolds shear stress profiles in the separated turbulent boundary layer as

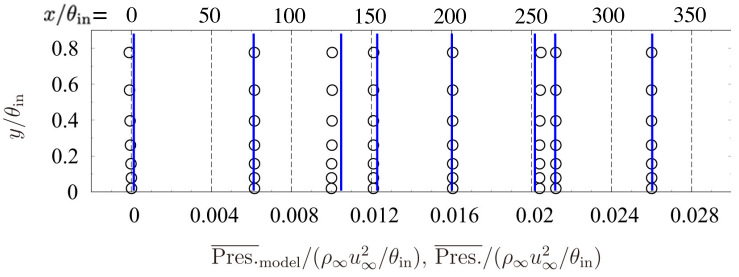

(a) Pressure gradient term (each profile is separated by a horizontal offset of 0.004)

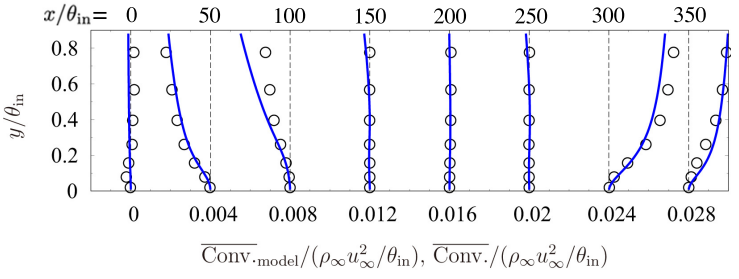

(b) Convective term (each profile is separated by a horizontal offset of 0.004)

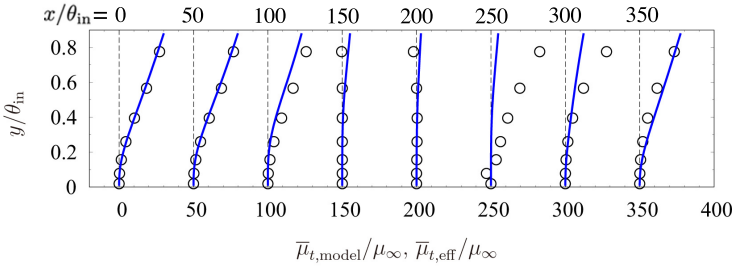

(c) Turbulent eddy viscosity (each profile is separated by a horizontal offset of 50)

FIG. 14. Modeled nonequilibrium terms in the separated and reattached turbulent boundary layer. Blue lines, proposed ODE-based NEQBL wall model; circles, WRLES database [29].

accurately as the existing PDE-based NEQBL model. The results suggest that the proposed ODE-based NEQBL wall model can be used as an alternative to the existing PDE-based NEQBL wall model. Considering the need to solve the time-dependent PDE equations on the computational grids with full connectivity in the existing PDE-based NEQBL model, the proposed ODE-based NEQBL model extends the applicability of the WMLES to flow simulations around complex geometries.

ACKNOWLEDGMENTS

This work was supported in part by JSPS KAKENHI Grants No. 18H01620 and No. 21H01523. A part of this research used computational resources of the ITO computer, provided by the Research Institute for Information Technology, Kyushu University (Project ID No. hp200012) and

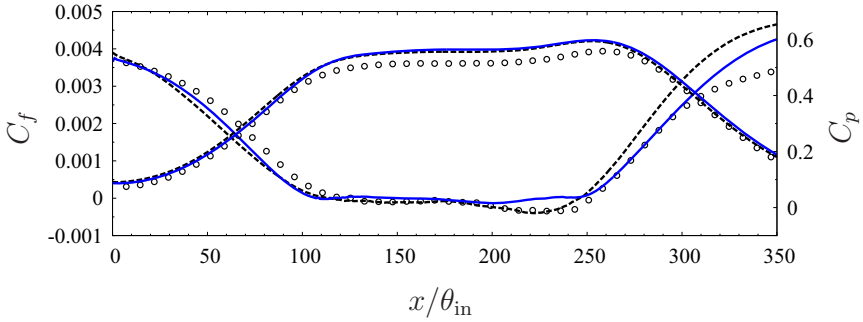

FIG. 15. Skin friction coefficient C_f and wall pressure coefficient C_p ($C_f \approx 0.004$ and $C_p \approx 0.1$ at $x/\theta_{\rm in} = 0$). Blue lines, proposed ODE-based NEQBL wall model; black dashed-lines, PDE-based NEQBL wall model [13]; circles, WRLES database [29].

supercomputer Fugaku provided by RIKEN Center for Computational Science (Projects ID No. hp210099 and ID No. hp220034).

APPENDIX: INCORPORATING THE EFFECTS OF PRESSURE GRADIENT INTO WALL-DAMPING FUNCTION IN TURBULENT EDDY VISCOSITY MODEL

As discussed in Sec. II B 3, in the proposed turbulent eddy viscosity in the ODE-based NEQBL wall model, the eddy viscosity is modeled as

$$\frac{\overline{\mu}_{t,\rm model}}{\overline{\mu}_w} \approx \kappa y^* D^*, \;\; D^* = \left[1 - \exp\left(-\frac{y^*}{A}\right)\right]^\beta, \tag{A1}$$

where $\kappa = 0.41$, $A = 17$, and $\beta = 2$. The values of the coefficients κ and A are calibrated for the equilibrium boundary layer. However, there is no guarantee that those values are valid even in nonequilibrium flows. For example, the wall-damping function of the turbulent eddy viscosity may change due to the adverse pressure gradient. As shown in Fig. 7, scaling the turbulent eddy viscosity by y^* is reasonably accurate in the log layer, while the possibility of improving the wall-damping function in the viscous layer remains. Therefore, in this Appendix, the sensitivity of the wall-damping function in the turbulent eddy viscosity model is investigated by *a priori* tests using the WRLES database, seeking a possible improvement by taking the effects of pressure gradient into account.

Here, we consider the nondimensionalized pressure $p^+ \equiv [\nu_w/(\rho_w u_\tau^3)](dp/dx)_w$ to incorporate the effects of pressure gradient into the wall damping function. Specifically, the wall damping of the turbulent eddy viscosity is designed to decrease in the region where p^+ is large (i.e., the damping constant A becomes small when the pressure-gradient is large). In this study, the following equation for A is examined:

$$A = 17[\exp(-|p^+|)]^3 + \epsilon, \tag{A2}$$

where if the pressure gradient $|p^+|$ is large, then the constant A reduces, and if the pressure gradient is zero, then Eq. (A2) becomes the original $A = 17$. ϵ is the small positive constant to prevent division by zero.

To decrease the wall damping in the region where p^+ is large, another possibility is to reduce the exponent β in the wall-damping function in Eq. (A1). One example of the modified wall-damping function considered in this study is

$$\beta = 2 - \min(\log|1 + 10p^+|,\; 2), \tag{A3}$$

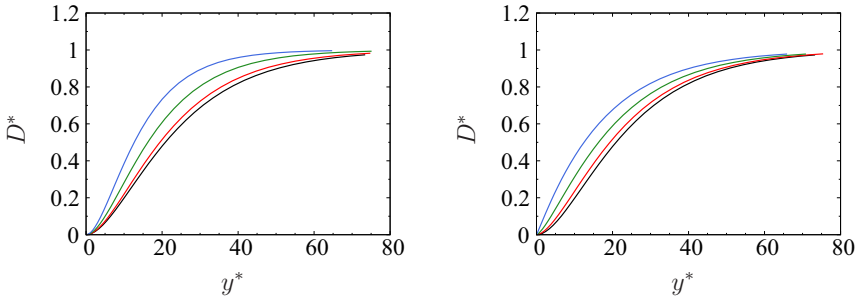

(a) Eq. (35) with the modified constant A (Eq. (36))

(b) Eq. (35) with the modified exponent β (Eq. (37))

FIG. 16. Behaviors of the modified wall-damping function in turbulent eddy viscosity model. Black lines, $x/\theta_{\rm in} = 0$; red lines, $x/\theta_{\rm in} = 50$; green lines, $x/\theta_{\rm in} = 75$; blue lines, $x/\theta_{\rm in} = 87.5$.

where if p^+ is large, β reduces, and $\beta = 2$ when $p^+ = 0$ (zero pressure gradient). The modified wall-damping functions [Eq. (A1) using the modified constant A in Eq. (A2) and Eq. (A1) with the modified exponent β in Eq. (A3)] at the adverse pressure-gradient region ($x/\theta_{\rm in} = 0$, 50, 75, 87.5) are shown in Fig. 16. Both the modified wall-damping functions decrease the wall damping as intended.

The skin friction predicted by the proposed ODE-based NEQBL wall model with the modified wall-damping functions is investigated through *a priori* tests by using the WRLES database. Figure 17 compares the skin friction predicted by the original damping function [$A = 17$ and $\beta = 2$ in Eq. (A1)] with those with the wall-damping function with the modified A [Eq. (A2)] and the exponent β [Eq. (A3)]. In the cases with the modified damping functions, the predicted skin friction approaches the reference WRLES database under the adverse pressure gradient ($30 \lesssim x/\theta_{\rm in} \lesssim 120$). For future work, additional investigations of the theoretical background are desired.

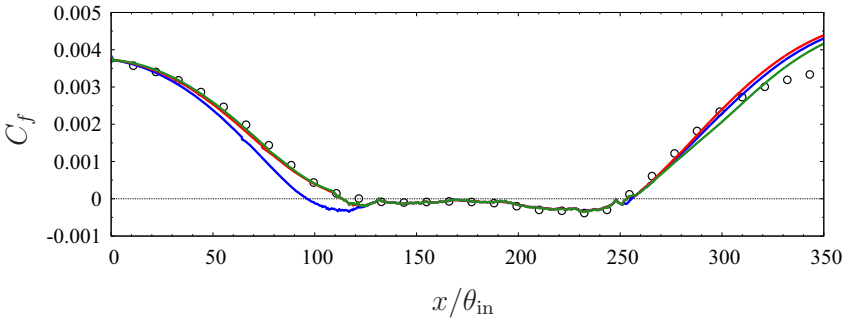

FIG. 17. Skin friction predicted by *a priori* test of proposed ODE-based NEQBL wall model with modified wall-damping function. Blue line, original damping function with $A = 17$ and $\beta = 2$ in Eq. (A1); red line, with modified constant A [Eq. (A2)]; green line, with modified exponent β [Eq. (A3)]; circles, WRLES database [29].

[1] D. R. Chapman, Computational aerodynamics development and outlook, AIAA J. **17**, 1293 (1979).
[2] H. Choi and P. Moin, Grid-point requirements for large eddy simulation: Chapman's estimates revisited, Phys. Fluids **24**, 011702 (2012).
[3] J. Slotnick, A. Khodadoust, J. Alonso, D. Darmofal, W. Gropp, E. Lurie, and D. Mavriplis, CFD vision 2030 study: A path to revolutionary computational aerosciences, NASA Technical Report No. 2014–218178 (NASA, 2014).
[4] U. Piomelli and E. Balaras, Wall-layer models for large-eddy simulations, Annu. Rev. Fluid Mech. **34**, 349 (2002).
[5] J. Larsson, S. Kawai, J. Bodart, and I. Bermejo-Moreno, Large eddy simulation with modeled wall-stress: Recent progress and future directions, Mech. Eng. Rev. **3**, 15-00418 (2016).
[6] S. T. Bose and G. I. Park, Wall-modeled large-eddy simulation for complex turbulent flows, Annu. Rev. Fluid Mech. **50**, 535 (2018).
[7] J. W. Deardorff, A numerical study of three-dimensional turbulent channel flow at large Reynolds number, J. Fluid Mech. **41**, 453 (1970).
[8] U. Schumann, Subgrid scale model for finite difference simulations of turbulent flows in plane channels and annuli, J. Comput. Phys. **18**, 376 (1975).
[9] E. Balaras, C. Benocci, and U. Piomelli, Two-layer approximate boundary conditions for large-eddy simulations, AIAA J. **34**, 1111 (1996).
[10] W. Cabot and P. Moin, Approximate wall boundary conditions in the large-eddy simulation of high Reynolds number flow, Flow, Turbul. Combust. **63**, 269 (1999).
[11] M. Wang and P. Moin, Dynamic wall modeling for large-eddy simulation of complex turbulent flows, Phys. Fluids **14**, 2043 (2002).
[12] S. Kawai and J. Larsson, Wall-modeling in large eddy simulation: Length scales, grid resolution, and accuracy, Phys. Fluids **24**, 015105 (2012).
[13] S. Kawai and J. Larsson, Dynamic nonequilibrium wall-modeling for large eddy simulation at high Reynolds numbers, Phys. Fluids **25**, 015105 (2013).
[14] G. I. Park and P. Moin, An improved dynamic nonequilibrium wall-model for large eddy simulation, Phys. Fluids **26**, 015108 (2014).
[15] J. Lee, M. Cho, and H. Choi, Large eddy simulations of turbulent channel and boundary layer flows at high Reynolds number with mean wall shear stress boundary condition, Phys. Fluids **25**, 110808 (2013).
[16] I. Bermejo-Moreno, L. Campo, J. Larsson, J. Bodart, D. Helmer, and J. K. Eaton, Confinement effects in shock wave/turbulent boundary layer interactions through wall-modelled large-eddy simulations, J. Fluid Mech. **758**, 5 (2014).
[17] Y. Fukushima and S. Kawai, Wall-modeled large-eddy simulation of transonic airfoil buffet at high Reynolds number, AIAA J. **56**, 2372 (2018).
[18] A. Lozano-Duran, S. T. Bose, and P. Moin, Prediction of trailing edge separation on the NASA juncture flow using wall-modeled LES, AIAA Paper No. 2020–1776 (AIAA, Reston, VA, 2020).
[19] Y. Tamaki, Y. Fukushima, Y. Kuya, and S. Kawai, Physics and modeling of trailing-edge stall phenomena for wall-modeled large-eddy simulation, Phys. Rev. Fluids **5**, 074602 (2020).
[20] M. Cho, A. Lozano-Durán, P. Moin, and I. Park, Wall-modeled large-eddy simulation of turbulent boundary layers with mean-flow three-dimensionality, AIAA J. **59**, 1707 (2021).
[21] H. Asada, Y. Tamaki, R. Takaki, T. Yumitori, S. Tamura, K. Hatanaka, K. Imai, H. Maeyama, and S. Kawai, FFVHC-ACE: Fully automated Cartesian-grid-based solver for compressible large-eddy simulation, AIAA J. (article in advance), doi:10.2514/1.J062593.
[22] Y. Tamaki, H. Asada, R. Takaki, and S. Kawai, Wall-modeled LES around the CRM-HL using fully automated Cartesian-grid-based flow solver FFVHC-ACE, AIAA Paper No. 2022–3454 (AIAA, Reston, VA, 2022).
[23] A. Lozano-Durán, S. T. Bose, and P. Moin, Performance of wall-modeled LES with boundary-layer-conforming grids for external aerodynamics, AIAA J. **60**, 747 (2022).
[24] S. Hickel, E. Touber, J. Bodart, and J. Larsson, A parametrized nonequilibrium wall-model for large-eddy simulations, in *CTR Proceedings of the Summer Program 2012* (Center for Turbulence Research, NASA Ames and Stanford University, 2012), pp. 127–136.

[25] G. I. Park, Wall-modeled large-eddy simulation of a high Reynolds number separating and reattaching flow, AIAA J. **55**, 3709 (2017).
[26] G. Hoffmann and C. Benocci, Approximate wall boundary conditions for large eddy simulations, in *Advances in Turbulence V* (Springer, Berlin, 1995).
[27] P. Catalano, W. Wang, G. Iaccarino, and P. Moin, Numerical simulation of the flow around a circular cylinder at high Reynolds numbers, Int. J. Heat Fluid Flow **24**, 463 (2003).
[28] Z. Zhou, G. He, and X. Yang, Wall model based on neural networks for LES of turbulent flows over periodic hills, Phys. Rev. Fluids **6**, 054610 (2021).
[29] S. Kawai, Kawai Lab. DNS/LES Database, Tohoku University, https://www.klab.mech.tohoku.ac.jp/database/.
[30] Y. Na and P. Moin, Direct numerical simulation of a separated turbulent boundary layer, J. Fluid Mech. **374**, 379 (1998).
[31] H. Abe, Reynolds-number dependence of wall-pressure fluctuations in a pressure-induced turbulent separation bubble, J. Fluid Mech. **833**, 563 (2017).
[32] G. N. Coleman, C. L. Rumsey, and P. R. Spalart, Numerical study of turbulent separation bubbles with varying pressure gradient and Reynolds number, J. Fluid Mech. **847**, 28 (2018).
[33] S. Kawai and S. K. Lele, Large-eddy simulation of jet mixing in supersonic crossflows, AIAA J. **48**, 2063 (2010).
[34] S. Kawai, Heated transcritical and unheated nontranscritical turbulent boundary layers at supercritical pressures, J. Fluid Mech. **865**, 563 (2019).
[35] G. Urbin and D. Knight, Large-eddy simulation of a supersonic boundary layer using an unstructured grid, AIAA J. **39**, 1288 (2001).
[36] S. Kawai and K. Fujii, Compact scheme with filtering for large-eddy simulation of transitional boundary layer, AIAA J. **46**, 690 (2008).
[37] P. Schlatter and R. Örlü, Assessment of direct numerical simulation data of turbulent boundary layers, J. Fluid Mech. **659**, 116 (2010).
[38] S. K. Lele, Compact finite difference schemes with spectral-like resolution, J. Comput. Phys. **103**, 16 (1992).
[39] D. V. Gaitonde and M. R. Visbal, Padé-type higher-order boundary filters for the Navier-Stokes equations, AIAA J. **38**, 2103 (2000).
[40] C. W. Shu and S. J. Osher, Efficient implementation of essentially nonoscillatory shock capturing schemes, J. Comput. Phys. **77**, 439 (1988).
[41] E. Lenormand, P. Sagaut, and L. Ta Phuoc, Large eddy simulation of subsonic and supersonic channel flow at moderate Reynolds number, Int. J. Numer. Methods Fluids **32**, 369 (2000).
[42] S. Hickel and N. A. Adams, Implicit LES applied to zero-pressure-gradient and adverse-pressure-gradient boundary-layer turbulence, Int. J. Heat Fluid Flow **29**, 626 (2008).
[43] H. Schlichting and K. Gersten, *Boundary-Layer Theory* (Springer, Berlin, 2016).